Evaluation of strain distribution in freestanding and buried lateral nanostructures

A. Ulyanenkov,* N. Darowski, J. Grenzer, and U. Pietsch†
Institute of Physics, University of Potsdam, Am Neuen Palais 10, D-14415 Potsdam, Germany

K. H. Wang and A. Forchel
Institute of Technical Physics, University of Würzburg, Am Hubland, D-97074 Würzburg, Germany
(Received 28 June 1998)

A free-standing lateral nanostructure based on GaAs[001] containing a $Ga_{0.97}In_{0.03}As$ single quantum well and similar structures after the overgrowth with GaAs and AlAs, respectively, have been investigated by high-resolution x-ray grazing incidence diffraction (GID) and conventional x-ray diffraction (HRXRD). The wire shape of the freestanding structure and the lateral density variation in the overgrown samples, were determined by running scans with constant length of the scattering vector (transverse scans) across the grating truncation rods (GTR's) close to the $(\bar{2}20)$ reflection. The in-plane strain distribution became available crossing the (220) GTR's by a scan in the longitudinal direction. Exploiting the capability of GID for depth resolution, the in-plane strain distribution was analyzed for different values of depth below the sample surface. The strain analysis was completed by HRXRD measurements close to the (004) reflection. The x-ray measurements were interpreted in terms of the distorted wave Born approximation applied for GID geometry. The strain distribution is determined by comparing the measured GTR intensities with the corresponding simulations containing the displacement fields obtained from finite-element calculations. At the freestanding wire structure we find laterally compressive strain of about $\Delta a/a_{\parallel} = -2\times10^{-3}$ at the single quantum well (SQW) with a steep strain gradient close to the wire side walls. Both overgrown samples show pronounced lateral strain variation within the overgrown layer, which still appears up to the completely planar surface. Within the SQW the in-plane strain is still compressive after GaAs overgrowth and of similar amount compared to the freestanding grating. The strain is increased by about 30% after overgrowth with AlAs. For both overgrown samples the strain gradient near the wire side walls is reduced, but reaches a maximum close to the SQW. Accompanied by the defect passivation, these findings explain the difference in the energy shift of the photoluminescence line between freestanding and overgrown lateral nanostructures. [S0163-1829(99)08047-9]

I. INTRODUCTION

In addition to varying chemical composition the electronic band gap of semiconductors can be modified by vertical and lateral patterning. Quantization along the growth direction is obtained by keeping the thickness of the active layer smaller than the excitonic radius of the particular material (single quantum well-SQW). The created atomiclike energy levels modify the electronic band gap that initiates a blueshift of the photoluminescence (PL) signal. Because this energy shift scales inversely with the thickness of the SQW the electronic properties can be tailored by controlled preparation.

Additional lateral patterning (quantum wires-QW) increase the density of states close to the quantization levels of the SQW, increases the quantum efficiency of radiative recombination, and lowers the threshold of respective laser devices. Patterning in both lateral directions (quantum dots-QD) creates three-dimensional (3D) atomiclike aggregates on a mesoscopic level, which provides interesting new physical properties.[1]

The lattice relaxation of the lateral nanostructure modifies the electronic band gaps as well. Depending on the thickness ratio between active and confinement layers, the lateral lattice parameter of the QW in a freestanding structure is larger than that in a pseudomorphically strained structure. The induced shift of the electronic band levels is usually described by deformation potentials.[2] Up to now the relation between strain relaxation and the induced shift of the PL energy has been investigated only qualitatively. The PL shift as a function of the wire width has been observed for $GaAs/In_xGa_{1-x}As/GaAs[001]$ QW's.[3] As shown in Fig. 1 the PL line is redshifted for free-standing wire structures by decreasing the wire widths. In contrast, the overgrown samples show an opposite behavior. Upon decreasing the wire width, the PL-line is blueshifted. The blue shift is ex-

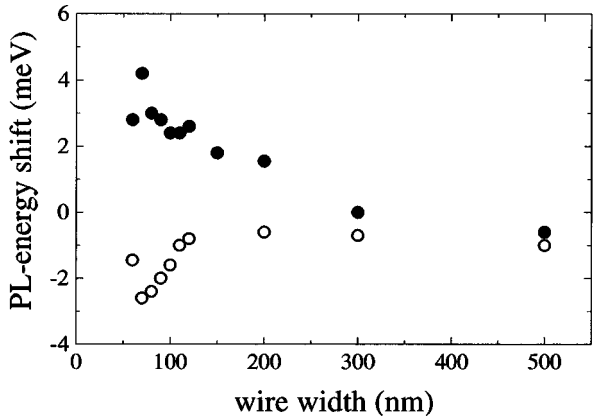

FIG. 1. PL-line shift of a series of free-standing and overgrown wires of a $GaAs/In_{0.14}Ga_{0.84}As/GaAs$ SQW structure, measured at 4 K. The overgrowth material is GaAs.

plained by lateral quantization; the redshift by the lattice relaxation of the freestanding wires with respect to the pseudomorphic strain state measured at the nonstructurized mesa. Comparing freestanding and overgrown samples, the PL-intensity was significantly enhanced in the case of latter, and the strain induced redshift was compensated after the overgrowth process.[4]

A deeper understanding of the relationship between the spatial strain distribution and the initiated shifts of related band levels would help to improve the quality and efficiency of laser devices. Due to the different geometry the relations between the strain and the band shift known for bulk or epitaxial materials cannot be transfered directly on lateral nanostructures. Therefore, nondestructive methods for strain analysis are required to be accompanied by numerical strain calculations to determine the 3D strain distribution close to the active SQW within a investigated nanostructure.

X-ray diffraction techniques are widely used for strain anlysis of epitaxial layer systems.[5] Modern x-ray equipments and high-power x-ray sources enable high resolution in reciprocal space and consequently a nondestructive determination of strains in a three-dimensional space. After the pioneering papers published by Tapfer and Holy,[6,7] Baumbach *et al.* introduced the method of reciprocal space mapping as an efficient tool for inspecting the strain distribution of lateral nanostructures[8] and Shen *et al.* presented the first quantitative in-plane strain analysis of surface nanostructures[9] interpreted by use of a geometric approach.

Due to the lateral patterning of the sample surface, satellite reflections appear close to any fundamental Bragg reflection of the substrate. Their angular distance is a measure for the inverse of the perodicity D of the patterning. The one-dimensional truncation of the infinite 3D space by the sample surface leads to an extension of the Bragg intensities along the surface normal. A systematic inspection of these crystal truncation rods (scan across the fundamental Bragg peak) and the grating truncation rod intensities (across the satellite peaks) provides information about the shape and the residual strain in QW's.[10] Accompanied with finite-element calculations and numerical rocking-curve simulations based on the semikinematic approximation for the x-ray scattering process, the determination of the 3D strain distribution across the nanostructure becomes available. The capability of this technique was recently demonstrated.[11] Using high-resolution coplanar x-ray diffraction the authors evaluated the strain distribution in $InP/In_xGa_{1-x}AsP/InP$ lateral nanostructures and analyzed a correlation of their results to optical properties of the respective wire laser structure.

Besides high-resolution x-ray diffraction (HRXRD), noncoplanar grazing incidence diffraction is an efficient tool for in-plane strain analysis.[12] Exploiting refraction of the incident beam at the sample surface, the penetration depth of the beam into the sample can be changed in the range between 5 nm and several 100 nm. This enables an evaluation of the vertical variation of the in-plane strain acting at the quantum wires. For $[1\bar{1}0]$ oriented wires on cubic substrates, both strain and wire shape influence the recorded rocking curves. These contributions can be separated by the inspection of two symmetry-equivalent in-plane Bragg reflections.[13]

This technique was applied to investigate the strain distribution in free-standing $In_xGa_{1-x}AsP/InP[001]$ quantum wire structures.[11] Combining the curve simulations in terms of the distorted wave Born approximation (DWBA) and finite-element calculations, we found a quantitative correlation between the residual in-plane strain and the PL-energy of $GaAs/In_xGa_{1-x}As/GaAs$ nanostructures.[14] Furthermore, we found a periodic strain modulation for the first time in an almost homogeneous $Al_xGa_{1-x}As$ layer overgrown onto a GaAs lateral wire structure.[15] This periodic strain distribution may suppress the strain relaxation within the SQW and has to be considered for device optimization.

The aim of this paper is the systematic analysis of the strain distribution in $GaAs/In_xGa_{1-x}As/GaAs$ wire structures before and after overgrowth with AlAs and GaAs composites. The In concentration ($x=3\%$) is small enough to prevent nonelastic strain release and strain-induced defect generation. We combine HRXRD and grazing incidence diffraction (GID) to determine the out-of-plane and the in-plane strain components separately; the latter one is considered as a function of depth below the sample surface. The experimental rocking curves are analyzed taking into account the displacement fields calculated by using a finite-element approach based on linear elasticity theory. The adaptation of parameters to the experiment is performed by refining a model structure. Using a deformation potential approach, the evaluated strain distribution is discussed in terms of its consequence for strain-induced band-gap variations explaining respective PL measurements. The paper is organized as follows: first we explain the experimental techniques used (Sec. II), then we present the DWBA approach for analyzing the data (Sec. III) and the experimental results (Sec. IV). Finally, we discuss the results in terms of the displacement field calculated by finite element method (FEM) and discuss the respective consequencies for the optical properties.

II. SAMPLE PREPARATION AND EXPERIMENTS

A. Sample preparation

A series of $GaAs/In_xGa_{1-x}As/GaAs$ single-quantum well structures with an additional one-dimensional lateral patterning was prepared. The principal structure of the samples is shown in Fig. 2.

For all three samples the vertical structure was grown first by solid source molecular beam epitaxy (MBE). A 200-nm thick GaAs buffer layer was deposited on a GaAs (001) substrate, followed by a $t_{SQW}=5$ nm-thick $Ga_{0.97}In_{0.03}As$ single-quantum well, and capped by a GaAs layer with a nominal thickness of $t_{top}=20$ nm.

The lateral patterning of this layered structure was carried out by a lithography process and subsequent etching. The spin-coated positive photoresist polymethylmethacrylate was exposed by an electron beam using a commercial E-Beam (EIKO) and then developed. The deposition of a thin (6 nm) aluminum layer and a subsequent lift-off process defined a metallic etch mask. The pattern, a one dimensional grating along the $[1\bar{1}0]$ direction with a periodicity $D=250$ nm and a nominal wire width of $t_{top}=95$ nm, was transferred onto the semiconductor material by wet chemical etching using 1:1:60 $H_3PO_4:H_2O_2:CH_3OH$ at 21 °C at a rate of 20 nm/min. The etching depth t, i.e., the sum over t_{top}, t_{SQW} and the bottom part of the grating t_{bot}, which corresponds to the

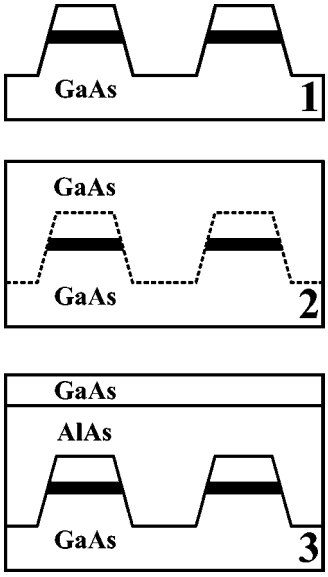

FIG. 2. Sketch of the investigated series of samples showing the principle shape and deposited materials. The shaded area shows the position of the $In_{0.03}Ga_{0.97}As$ single-quantum well.

depth etched into the buffer layer, amounts to 60 nm for all samples, as found by a morphology profiler (DEKTAK). Wet chemical etching instead of the anisotropic reactive ion-beam etching was used because it produces less damaged side walls, essential for high-optical quality. Due to this choice the defined grating finally shows trapezoidal shape with (111) facets as side walls. In addition to the grating arrays with a size of 2000 μm$\times$400 μm, two-dimensional reference (mesa) fields of 100 μm$\times$100 μm were realized on each sample. This enabled us to obtain photoluminescence data as a function of the strain present in the grating structure for direct comparison with a laterally unpatterned reference.

Of special interest was the change of the strain distribution within the partially relaxed wires after the overgrowth with material of different lattice parameters. Thus two of the three samples were overgrown with GaAs and AlAs, respetively, using an additional MBE step. In the following we refer to the freestanding sample as Sample 1, the overgrown ones by Sample 2 (GaAs overgrowth), and Sample 3 (AlAs overgrowth). The nominal thickness of this overlayer is $t_{\mathrm{over}}=100$ nm in both cases. In case of Sample 3 a cap layer with the thickness of $t_{\mathrm{cap}}=10$ nm had to be deposited to protect AlAs from oxidation.

The geometrical parameters introduced in this section are illustrated in Fig. 3.

B. Diffraction techniques

All x-ray measurements have been performed by running particular line scans in reciprocal space. The three coordinates of the reciprocal space inside the sample are defined as follows:

$$q_{\mathrm{x}}=\frac{2\pi}{\lambda}(\cos\alpha_{\mathrm{f}}\cos\vartheta_{\mathrm{f}}-\cos\alpha_{\mathrm{i}}\cos\vartheta_{\mathrm{i}}) \tag{1}$$

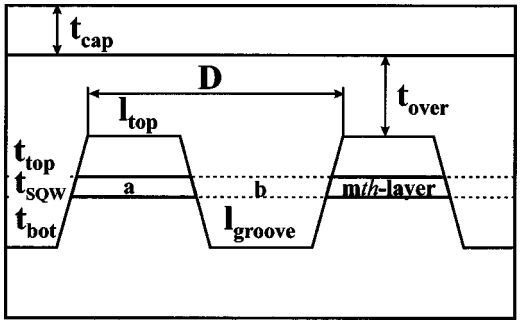

FIG. 3. Sketch of an overgrown grating structure denoting the relevant geometric parameters used for the simulation of the x-ray measurements.

$$q_{\mathrm{y}}=\frac{2\pi}{\lambda}(\cos\alpha_{\mathrm{f}}\sin\vartheta_{\mathrm{f}}+\cos\alpha_{\mathrm{i}}\sin\vartheta_{\mathrm{i}}) \tag{2}$$

$$q_{\mathrm{z}}=\frac{2\pi}{\lambda}(\sqrt{\sin^2\alpha_{\mathrm{f}}-\sin^2\alpha_{\mathrm{c}}}+\sqrt{\sin^2\alpha_{\mathrm{i}}-\sin^2\alpha_{\mathrm{c}}}), \tag{3}$$

Here, $\alpha_{\mathrm{i,f}}$ denote the incident and exit angle with respect to the sample surface, $\vartheta_{\mathrm{i,f}}$ refer to the in-plane angles with respect to the diffracting lattice plane (Fig. 4), and α_{c} is the critical angle of total external reflection, which for GaAs and $\lambda=0.124$ nm amounts to 0.253°. Considering the crystallographic alignment of wires ($\|[\bar{1}10]$), we introduce two reciprocal vectors in addition; the $q_{\perp}$ axis is set parallel to $[110]$ and $q_{\|}$ parallel to $[\bar{1}10]$. q_{z} coincides with the surface normal in direct space, i.e., the $[001]$ direction. Using this setup, the satellite peaks occuring due to the one-dimensional patterning of the surface are expected when scanning along $q_{\perp}$.

Scans in coplanar scattering geometry (HRXRD) were performed in the $(q_{\mathrm{x}},q_{\mathrm{z}})$ plane. For the considered symmetric (004) reflection the diffracting lattice plane lies parallel to the sample surface, therefore $\vartheta_{\mathrm{i,f}}$ become zero and only

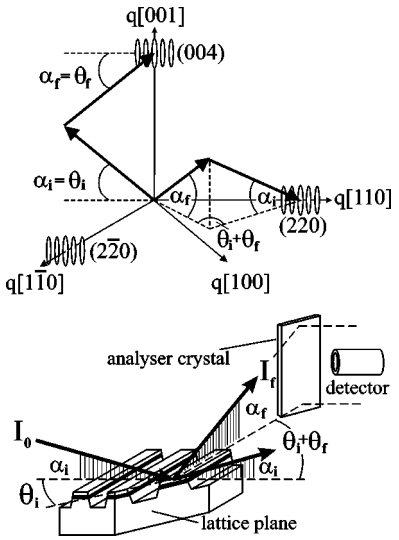

FIG. 4. (a) Sketch of the reciprocal space showing the recorded RLP's and the corresponding geometry. (b) Detailed GID setup with all relevant angles depicted.

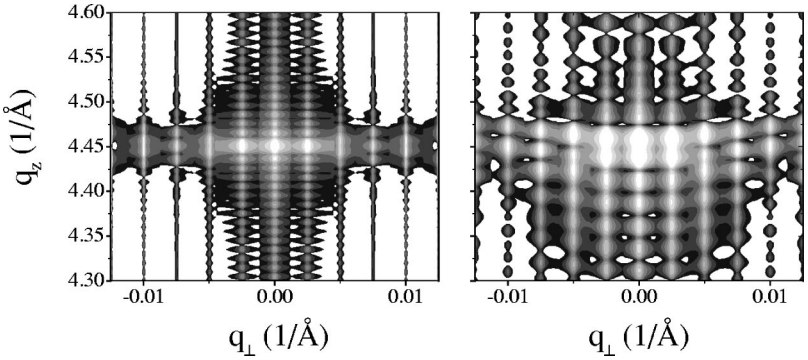

FIG. 5. Simulation of the intensity distribution around the symmetric (004) reflection without (a) and with (b) consideration of the displacement field of sample 1 calculated by FEM. The 8 contour lines are plotted on logarithmic scale from 1×10^{-11} to 1×10^{-6}.

$\alpha_{i,f}$ have to be changed. Because both angles are large (about 20°), the influence of refraction can be neglected for the calculation of q_z.

In the noncoplanar GID geometry the incoming beam strikes the sample surface with a grazing angle of incidence α_i, whereas the angle with respect to the diffracting lattice plane ϑ_i is measured in plane. A diffracted beam occurs under a grazing angle of exit with respect to the sample surface α_f at the detector position $\vartheta_i+\vartheta_f=2\vartheta_{Bragg}$ whenever an in-plane Bragg reflection becomes adjusted by rotating the sample around its surface normal, as depicted in Fig. 4. Thus, line scans performed with this setup run in the (q_x,q_y) plane with small and fixed q_z. q_z scans (rod scans) were recorded at the particular $q_\perp$ positions of satellites. Following Eqs. (1)–(3), four angles can be changed to vary three reciprocal space coordinates. This gives us the opportunity to keep one of the angles fixed. We set α_i fixed to define a particular information depth for each line scan. Similar scans recorded at different q_z provide depth resolution.

The information depth Λ is defined as the decay length of the probing x-ray beam below the sample surface. It becomes evanescent under condition of total external reflection. Λ is given by the reciprocal of the imaginary part of q_z

$$\frac{1}{\Lambda}=\Im q_z=\frac{1}{\Lambda_i}+\frac{1}{\Lambda_f}, \tag{4}$$

using

$$\Lambda_{i,f}=\frac{\lambda}{2\sqrt{2}\pi\{\sqrt{(\alpha_{i,f}^2-\chi_0')^2+4\chi_0''^2}-(\alpha_{i,f}^2-\chi_0')\}^{1/2}}. \tag{5}$$

χ_0' and χ_0'' denote the real and imaginary part of the dielectric susceptibility modifying the x-ray refractive index to $n=1-\chi_0'/2+i\chi_0''/2$. Keeping the angle of incidence with respect to the sample surface smaller than the criticle angle of total external reflection α_c, the value of Λ_i is limited to few nanometers. In the case of $\alpha_i>\alpha_c$, the penetration depth approaches several hundreds of nanometers and is only canceled by the imaginary part χ_0'', which is linearly proportional to the absorption coefficient μ.[5] In the HRXRD setup Λ_i always exceeds several hundred nanometers and provides depth-averaging information only.

An additional advantage of GID geometry is the possibility to separate the influence of the displacement field and the grating shape on measured x-ray diffraction curves. For wire structures we expect relaxation only along $q_\perp$, i.e., the direction of the lateral patterning, whereas the substrate lattice parameter is observable along the wires. Since the scattering experiment is only sensitive to lattice parameter variation if the momentum transfer is aligned solely along the relaxation direction, the longitudinal scan (q_y scan) shows the influence of strain in the recorded intensity distribution. Performing a transverse scan (q_x scan) the length of the scattering vector is nearly unchanged, thus this line scan is insensitive to the in-plane strain and displays only the influence of shape. Therefore, we are able to separate the contributions of both effects, strain and shape, by recording the intensity pattern around two symmetrically equivalent in-plane reflections, the strain sensitive (220) and the strain insensitve $(\bar{2}\bar{2}0)$.[13]

The GID measurements have been performed with the diffractometer in *z*-axis geometry at experimental station ID03 at the ERSF (Grenoble, France) using a wavelength of $\lambda=0.1218$ nm, whereas the coplanar high-resolution x-ray diffraction experiments were carried out at the wiggler beamline BW2 at HASYLAB (Hamburg, Germany) using a wavelength of $\lambda=0.124$ nm. Both experimental stations are equipped with a silicon(111) double crystal monochromator. High resolution in reciprocal space was achieved by mounting a silicon(111) analyzer crystal in front of the scintilation detector, resulting in an in-plane resolution Δq better than 10^{-4}.

C. Strain influence

As it clearly can be seen in Fig. 5, the presence of strain within the structure dramatically changes the intensity distribution around the fundamental Bragg reflections in reciprocal space. The displacement field of Sample 1, which is considered for the simulation of these maps is calculated by the commercial software MARC 7.0 using the finite element method. The geometrical structure is divided into small elements of appropriate size and shape (8-node cuboid or in a more general case 8-node truncated pyramidal-shaped body) for which the physical quantity of interest is calculated iteratively up to a termination condition defined by a maximum deviation between neighboring nodes. The periodicity of the grating is taken into account by the boundary conditions. What means, no displacement is considered along $[\bar{1}10]$ for all nodes, along $[110]$ (i.e., the replication direction of the grating) for the nodes belonging to the left and right boundaries of the bulk and along $[001]$ (i.e., the growth direction) for the nodes belonging to the bottom boundary of the defined substrate layer. As the driving force for relaxation the relative lattice constant difference, i.e., the misfit *f*, of the

deposited layers with respect to the GaAs substrate ($f=0$) is considered. The results of the calculation that is used for the interpretation of the measured x-ray intensities are *two of the* six components of the strain tensor, $\epsilon_{xx}(x,z)$ and $\epsilon_{zz}(x,z)$, and the displacements $\delta x(x,z)$ and $\delta z(x,z)$ along the $[\bar{1}10]$ and $[001]$ direction, respectively. The latter ones are used for the simulation of the x-ray measurements.

III. THEORETICAL CONSIDERATION

Lateral surface gratings, such as quantum wires, give rise to structurized x-ray diffraction pattern. Both for coplanar and grazing incidence geometries, equidistant diffraction maxima appear due to the lateral periodicity of the wires. These maxima have a fine structure which reflects the detailed geometrical shape of the wires and the strain status of the crystallographic lattice. In principle, the diffraction curves of GID from nanostructures contain direct information on the shape and strain distribution within the QW, providing the possibility of a complete study of a sample by a single method.

We use the distorted-wave Born approximation for a theoretical description of the diffraction process on the multilayered surface and buried gratings. To take into account the double-diffraction effects, the perturbation theory was extended up to second order, by analogy with Ref. 18. This approach was already used for the calculation of conventional x-ray diffraction and x-ray reflectometry pattern.[8,16]

The lattice and wire imperfections cause diffuse scattering accompanying the coherent component of the output intensity. The incoherent component contains certain information about QW shape fluctuations,[17] and interface,[19,20] and lattice imperfections.[21] Although this component is clearly visible in some of the experiments presented here, we simulated our theoretical curves in the coherent approximation to distinguish the principal features of the applied method. The diffuse scattering from surface gratings is the subject of forthcoming investigations. Here, we discuss qualitatively the sample imperfections giving rise to the diffuse component in the diffraction signal.

The scattering of x-rays from investigated structures is described by the wave equation (we consider here σ polarization of x-rays)

$$(\Delta + K^2)\,\psi(\mathbf{r}) = V(\mathbf{r})\,\psi(\mathbf{r}). \tag{6}$$

The incident wave Φ with vacuum wave vector K being scattered by an optical potential V originates the wave $\psi(\mathbf{r})$, which can be written in general as

$$\psi(\mathbf{r}) = \Phi(\mathbf{r}) + \int d\mathbf{r}'\, G_0(\mathbf{r},\mathbf{r}')\, V(\mathbf{r}')\,\psi(\mathbf{r}'), \tag{7}$$

with $G_0(\mathbf{r},\mathbf{r}')$ as the Green function of the free particle. By using the Heisenberg representation of quantum mechanics we express the solution of Eq. (6) in the complete orthogonal basis of solutions for the wave equation

$$(\Delta + K^2)\,\psi^{(0)}(\mathbf{r}) = V_1(\mathbf{r})\,\psi^{(0)}(\mathbf{r}), \tag{8}$$

where $\psi^{(0)}(\mathbf{r})$ is the distorted wave scattered by the potential V_1. This wave is considered further as the initial state for the scattering by the perturbation potential[22] $V_2 = V - V_1$. Following perturbation theory, the eigenfunction $\psi(\mathbf{r})$ can be expanded as the series

$$\psi(\mathbf{r}) = \psi^{(0)}(\mathbf{r}) + \psi^{(1)}(\mathbf{r}) + \psi^{(2)}(\mathbf{r}) + \cdots, \tag{9}$$

where high-order approximations to $\psi(\mathbf{r})$ are calculated by means of the recursion formula

$$\psi^{(n)}(\mathbf{r}) = \int d\mathbf{r}'\, G_1(\mathbf{r},\mathbf{r}')\, V_2(\mathbf{r}')\,\psi^{(n-1)}(\mathbf{r}') \tag{10}$$

with $G_1(\mathbf{r},\mathbf{r}')$ as the Green function of a particle interacting with the potential V_1.

Let us now consider the multilayered gratings (Fig. 3), which can be buried within the structure, in general case. The nonperturbed potential within layer m $V_1^{(m)}$ is chosen to be proportional to the mean electric susceptibility of this layer

$$V_1^{(m)} = -K^2\langle\chi_0^{(m)}\rangle = \chi_{0a}^{(m)}\Omega_a^{(m)}(\mathbf{r}) + \chi_{0b}^{(m)}\Omega_b^{(m)}(\mathbf{r}). \tag{11}$$

Here the susceptibilities $\chi_{0a}^{(m)}$ and $\chi_{0b}^{(m)}$ correspond to regions a and b (Fig. 3), respectively, which can be filled by materials with different refractive properties. The heavy-side functions $\Omega_a^{(m)}(\mathbf{r})$ and $\Omega_b^{(m)}(\mathbf{r})$ describe the geometrical configuration of layer segments and are expressed by the heavy-side function of grating shape $\Omega_{SG}(\mathbf{r}_\parallel, z)$ and the function $\Omega_{ML}^{(m)}(z)$ defining a vertical multilayered structure.

$$\begin{aligned}\Omega_a^{(m)}(\mathbf{r}) &= \Omega_{SG}^{(m)}(\mathbf{r}_\parallel, z)\,\Omega_{ML}^{(m)}(z);\\ \Omega_b^{(m)}(\mathbf{r}) &= [1 - \Omega_{SG}^{(m)}(\mathbf{r}_\parallel, z)]\,\Omega_{ML}^{(m)}(z).\end{aligned} \tag{12}$$

We have chosen the perturbation potential V_2 in the form

$$V_2^{(m)} = -K^2 e^{i\mathbf{h}(\mathbf{r}-\mathbf{u}^{(m)}(\mathbf{r}))}[\chi_{ha}^{(m)}\Omega_a^{(m)} + \chi_{hb}^{(m)}\Omega_b^{(m)}] \equiv -K^2\chi_{GID}^{(m)}. \tag{13}$$

Here, we introduced the susceptibilities of regions a and b of layer m for grazing incidence diffraction on reciprocal lattice vector $\mathbf{h}$. The vector functions $\mathbf{u}^{(m)}(\mathbf{r}) = \mathbf{u}_0^{(m)}(\mathbf{r}) + \Delta\mathbf{u}^{(m)}(\mathbf{r})$ are the atom displacement functions describing the elastic deformation of the lattice structure and consisting of an undisturbed part $\mathbf{u}_0^{(m)}(\mathbf{r})$ originated during the epitaxial growth and displacements $\Delta\mathbf{u}^{(m)}(\mathbf{r})$ caused by grating-induced periodic distortions during the etching process.

Due to the periodicity, the susceptibility $\chi_{GID}^{(m)}$ of layer m can be expanded into the series

$$\chi_{GID}^{(m)}(\mathbf{r}) = e^{i\mathbf{h}(\mathbf{r}-\mathbf{u}_0^{(m)}(\mathbf{r}))}\sum_H \tilde{\chi}_{h,H}^{(m)}(z)\,e^{i\mathbf{H}\mathbf{r}_\parallel} \tag{14}$$

with Fourier components

$$\begin{aligned}\tilde{\chi}_{h,H}^{(m)}(z) = {}& \frac{\chi_{ha}^{(m)}}{D}\int_{-D/2}^{D/2} dx\;\; e^{-i\mathbf{H}\mathbf{r}_\parallel} e^{-i\mathbf{h}\Delta\mathbf{u}^{(m)}(\mathbf{r})}\Omega_a^{(m)}(\mathbf{r})\\ &+ \frac{\chi_{hb}^{(m)}}{D}\int_{-D/2}^{D/2} dx\;\; e^{-i\mathbf{H}\mathbf{r}_\parallel} e^{-i\mathbf{h}\Delta\mathbf{u}^{(m)}(\mathbf{r})}\Omega_b^{(m)}(\mathbf{r}),\end{aligned} \tag{15}$$

where the vector $\mathbf{H} = (2\pi/D)\mathbf{e}_x$ is the reciprocal grating vector and $\mathbf{e}_x$ is the unit vector in the x direction. The reciprocal grating vector describes the grating truncation rods, the two-

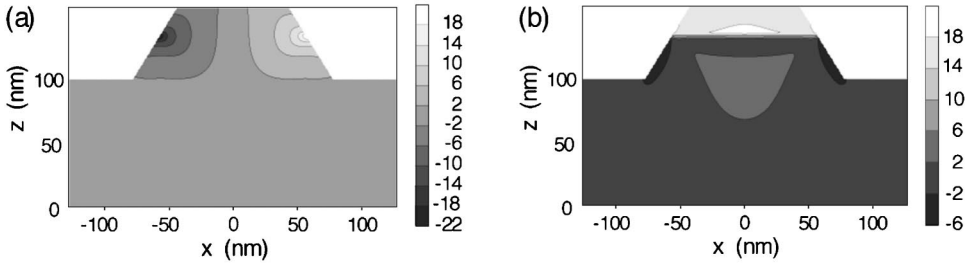

FIG. 6. FEM calculation of the displacements δx (a) and δz (b) of the freestanding grating (sample 1). The limits of the contour bands are given in units of 10^{-3} nm.

dimensional diffraction pattern formed by the scattering process on the periodic grating mesostructure. The position of GTRs in reciprocal space is defined by the condition for the scattering vector $\mathbf{Q}_\parallel = \mathbf{K}_{h\parallel} - \mathbf{K}_{0\parallel} = \mathbf{h}_\parallel + \mathbf{H}$ ($\mathbf{K}_0$ and $\mathbf{K}_h$ are wave vectors of incident and diffracted waves, respectively).

Here we drop the cumbersome explicit expressions for the diffracted wave amplitudes and refer the reader to the works.[8,5,23] For a simulation of the wave amplitudes, perturbation theory has been developed up to second order (9) giving a DWBA of second order. In this way the mutual interaction between the diffracted and reflected wave fields as well as the *Umweganregung* between the diffraction processes forming different GTR's are taken into consideration. The grating structure acts as transmission media both for incoming and outgoing (diffracted) waves. The changes in the intensity profile caused by such a twofold diffraction may be considerable in comparing with the theoretical treatment based on the first order distorted-wave Born approximation.[8] The structure amplitude of layer m corresponding to the reciprocal lattice vector $\mathbf{h}$ is composed of the scattering amplitudes of different GTR's

$$S_h^{(m)}(\mathbf{Q}) = 4\pi^2 \sum_H \delta(\mathbf{Q}_\parallel - \mathbf{h}_\parallel - \mathbf{H}) S_{h,H}^{(m)}(Q_z), \qquad (16)$$

where the amplitudes $S_{h,H}^{(m)}(Q_z)$ are defined by

$$S_{h,H}^{(m)}(Q_z) = e^{ih_z(z_m - u_{0z}^{(m)}(z_m))} \int_{z_m}^{z_{m+1}} dz \;\; \tilde{\chi}_{h,H}^{(m)}(z) e^{i(Q_z - h_z)(z - z_m)}. \qquad (17)$$

The values $\tilde{\chi}_{h,H}^{(m)}(z)$ for the freestanding wires (Sample 1) are calculated by Eq. (15), neglecting the second term. Formula (17) represents the contribution of one layer to the scattering amplitude of one grating truncation vector $\mathbf{H}$. To evaluate the total layer scattering amplitude, we replace the periodic grating shape function $\Omega_a^{(m)}(\mathbf{r})$ and grating-induced displacement function $U^{(m)}(\mathbf{r}) \equiv \exp[-i\mathbf{h}\Delta\mathbf{u}^{(m)}(\mathbf{r})]$ by their Fourier transforms

$$U^{(m)}(\mathbf{r}) = \sum_H U_H^{(m)}(z) e^{i\mathbf{H}\mathbf{r}_\parallel}, \quad \Omega_a^{(m)}(\mathbf{r}) = \sum_H \Omega_{aH}^{(m)}(z) e^{i\mathbf{H}\mathbf{r}_\parallel}. \qquad (18)$$

Upon substituting the expression (18) into Eq. (15), the layer scattering amplitude for freestanding wires is derived from Eq. (17):

$$\tilde{S}_H^{(m)}(Q_z) = \chi_{ha}^{(m)} \sum_{H'} \int dz \;\; e^{-iQ_z(z - z_m)} U_{H'}^{(m)}(z) \Omega_{aH-H'}^{(m)}(z). \qquad (19)$$

In the case of buried gratings (Samples 2 and 3), this function is modified to

$$\begin{aligned} \tilde{S}_H^{(m)}(Q_z) = (\chi_{ha}^{(m)} - \chi_{hb}^{(m)}) & \sum_{H' \neq H} \int dz \;\; e^{-iQ_z(z - z_m)} \\ & \times U_{H'}^{(m)}(z) \Omega_{aH-H'}^{(m)}(z) \\ & + \int dz \;\; e^{-iQ_z(z - z_m)} U_H^{(m)}(z) \langle \chi_h^{(m)} \rangle (z). \end{aligned} \qquad (20)$$

The first term in Eq. (20) is proportional to the compositional contrast $\chi_{ha}^{(m)} - \chi_{hb}^{(m)}$ between the segments of the (a) real and (b) ''inverted'' wires. The second term describes the scattering on the mean virtual layer with the susceptibility $\langle \chi_h^{(m)} \rangle$ averaged over the grating period.

As was mentioned in Sec. I, we expect the lattice displacements mainly in the vertical z direction and lateral x direction, neglecting the strain fields along the wires (y direction). Thus choosing the reciprocal lattice vector $\mathbf{h}$ to be perpendicular to displacement vectors $\mathbf{u}^{(m)}$ (i.e., parallelly to

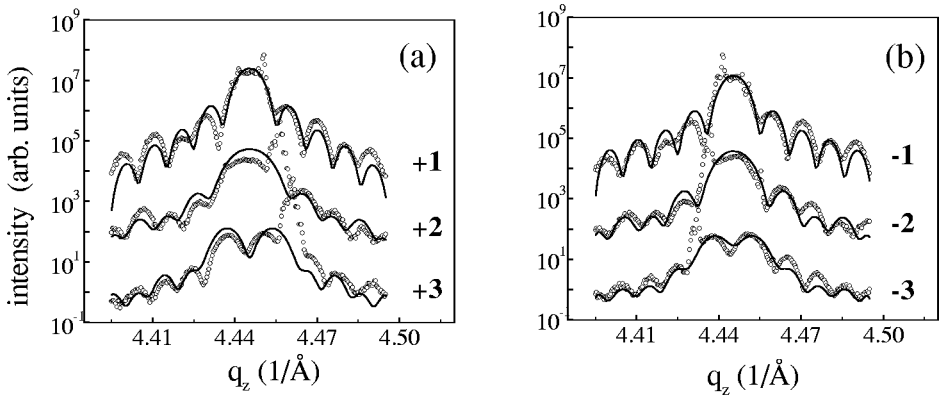

FIG. 7. Rod scans across the +1st to +3rd GTR (a) and −1st to −3rd GTR (b) recorded with HRXRD at the symmetrical (004) RLP of sample 1. The peak not described by theory is caused by the mirror used for collimation of the incident beam.

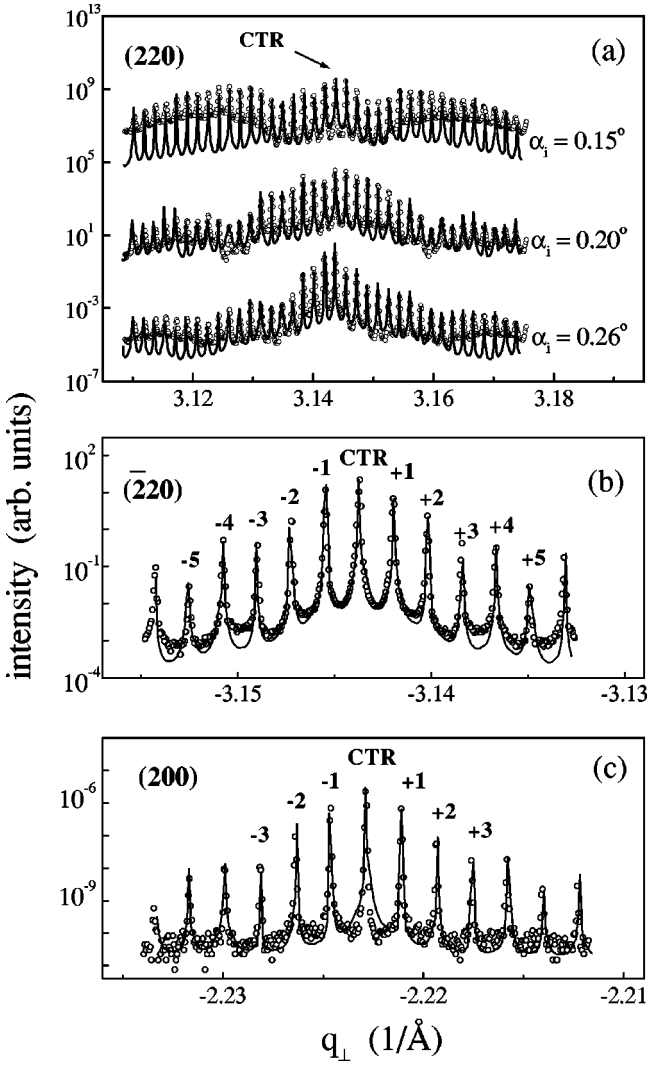

FIG. 8. In-plane scans for sample 1 recorded with GID from the both symmetry equivalent strong in-plane reflections, the longitudinal (220) RLP (a) and the transverse $(\bar{2}20)$ RLP (b) and from the weak (200) RLP (c).

y axis), the diffraction process is insensitive to the strain distribution within sample because all the vectors $U_{H'\neq 0}^{(m)}$ vanish. In our case this situation corresponds to diffraction on $(\bar{2}20)$ reflection (transverse scans), and from GTR's we obtain information about the shape and composition of wires. Conversely, longitudinal scans from the strong (220) reflection include information on both the shape and the strain. For Sample 2, the diffraction pattern from reflection (220) depends on the strain profile only because the wires being buried by the GaAs layer do not display their own geometrical shape. According to the theory developed above, the combination of longitudinal and transverse scans is believed to give complete knowledge about the strain profile, shape, and composition of freestanding and buried quantum wires. Moreover, the separation of the information in different types of scans simplifies the analysis of diffraction curves and eliminates ambiguity during the fitting of experimental data.

TABLE I. Fitted parameters

	Sample 1	Sample 2	Sample 3
Period D, Å	2550±49	2575±80	2568±55
l_{top}, Å	839±31	855±27	840±14
l_{groove}, Å	975±29	983±32	980±44
t_{top}, Å	212±18	230±23	205±15
t_{SQW}, Å	44±5	51±6	50±3
t_{bot}, Å	306±19	326±31	331±11
t_{over}, Å	—	413±36	~700
t_{cap}, Å	—	—	165±25

The coherent intensity of diffracted waves scattered by layer *m* to the position of the GTR in reciprocal space is proportional to

$$W_h^{(m)}(Q_z) = -K^2[T_0^{(m)}S_h^{(m)}(q_{z0}^{(m)})T_h^{(m)} + R_0^{(m)}S_h^{(m)}(q_{z1}^{(m)})T_h^{(m)} + T_0^{(m)}S_h^{(m)} - q_{z1}^{(m)})R_h^{(m)} + R_0^{(m)}S_h^{(m)}(-q_{z0}^{(m)})R_h^{(m)}]. \tag{21}$$

Here, the transmitted and reflected wave amplitudes $T_{0,h}^{(m)}$ and $R_{0,h}^{(m)}$ of incident and diffracted waves are calculated on the basis of the Fresnel formalism[24] for an undisturbed potential V_1. The values $q_{z0}^{(m)}$ and $q_{z1}^{(m)}$ are determined from

$$q_{z0}^{(m)} \equiv K_{zh}^{(m)} - K_{z0}^{(m)}; \quad q_{z1}^{(m)} \equiv K_{zh}^{(m)} + K_{z0}^{(m)}, \tag{22}$$

where the *z*-components of the wave vectors of incident and diffracted waves in layer *m* are related to the mean layer susceptibility (scattering by potential V_1) by

$$K_{hz}^{(m)} = \sqrt{K^2\langle\chi_h^{(m)}\rangle - K_{h\|}^2}; \quad K_{0z}^{(m)} = \sqrt{K^2\langle\chi_h^{(m)}\rangle - K_{0\|}^2}. \tag{23}$$

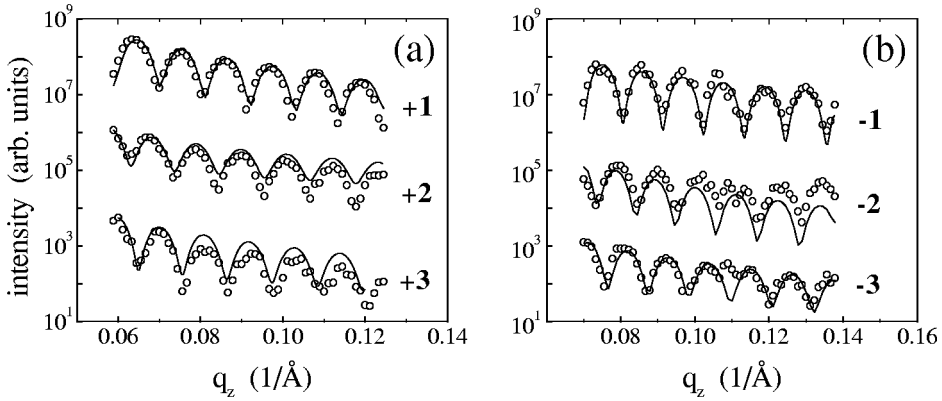

FIG. 9. Rods scans accross the +1st to +3rd GTR (a) and −1st to −3rd GTR (b) recorded with GID at the strain sensitive longitudinal (220) RLP of sample 1.

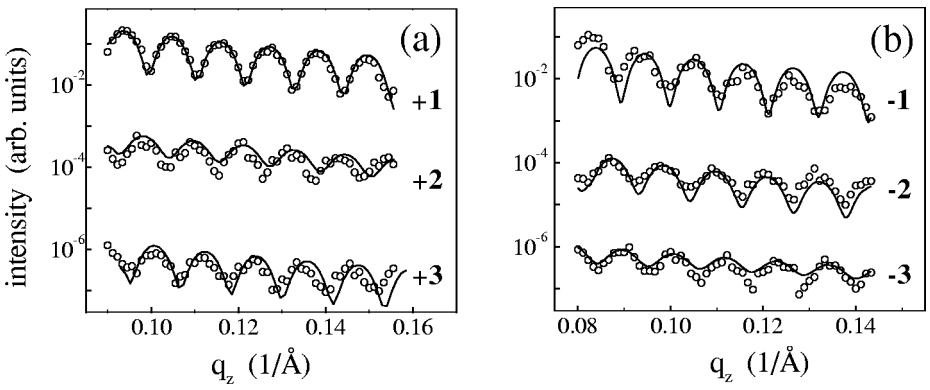

FIG. 10. Rods scans accross the +1st to +3rd GTR (a) and −1st to −3rd GTR (b) recorded with GID at the strain insensitive transverse $(\bar{2}20)$ RLP of sample 1.

As mentioned above, the diffuse component of x-ray scattering was not taken into account in our simulations. Some contribution of diffuse intensity is evident in the diffraction curves (Figs. 13 and 16) as a broadening of the peak bottoms and side wings that causes a slight discrepancy between theory and experiment. Certainly, the incoherent scattering brings valuable information on structure imperfections, a topic suitable for further investigation. The analysis of the diffusely scattered intensity is certainly useful[17] for studies on the fluctuation of wire height and period as well as the roughness of the side walls and the plane parts of the nanostructure. In our paper, we have emphasized the investigation of the strain profile and the general wires shape.

The considerable influence of the sample strain profile on the diffraction pattern is shown in Fig. 5. Two simulated reciprocal space maps around the reciprocal lattice point (004) are depicted for the freestanding wires which are completely free of strains (a) and assuming the strain profile calculated by FEM (b). The composition and dimensions of the model used for calculations are identical to that for Sample 1 described in Sec. I.1. The evident qualitative changes in the distribution of the diffracted intensities are expected to be the basis for the development of an effective method for investigation of the strain status of lateral gratings.

IV. EXPERIMENTAL RESULTS

A. Freestanding quantum wires

Since freestanding quantum wires with embedded SQW (Sample 1) represent the initial stage of the construction of structures with modulated strains, the detailed inspection of this sample is of special interest. The spatial strain distribution within the freestanding wires plays a key role in the formation of the strain profile of the final structure after subsequent overgrowing of the wires (Samples 2 and 3). Therefore, both HRXRD and GID analyses were carried out for this case. The strain profile simulated by FEM of a freestanding wire depicted in Fig. 6 clearly indicates the buried SQW as a perturbation center both for values δx and δz atom displacements. The maximal values of the displacements in the lateral direction δx are concentrated at the edges of SQW, and the vertical displacements δz have distinctly different signatures in the upper and lower parts of the wire segment with respect to the position of SQW. The magnitude of the displacements δx and δz reaches the maximal absolute values 0.220 and 0.189 Å, respectively and decrease rapidly below the bottom of the wires. Thus, the strains in the planar part of the samples can be neglected without loss in simulation accuracy. That the periodicity of the highly strained regions is connected to the periodicity of the wires, has certain influence both on the ordering and on the fine structure of the grating truncation rods. This is the reason for using of the simulated displacement profiles for the theorertical analysis of experimental diffraction curves in coplanar and grazing incidence geometries.

In the Figs. 7(a) and 7(b) we have plotted the measured (dots) and calculated (solid lines) HRXRD intensities around (004) reciprocal lattice point (RLP) for negative and positive GTR orders, respectively. The sharp peaks at the left (for negative GTR's) and right (for positive GTR's) sides of the fundamental Bragg peak are mirror streaks and do not contain any useful structural information. The acceptable agreement between experiment and theory shown in Fig. 7 is possible only when the real strain distribution (Fig. 6) is taken into account in the simulation of the diffraction process.

The fitting procedure both for HRXRD and GID patterns consisted of two steps. Firstly, the meshes of the atom displacements were simulated for the initial model with geo-

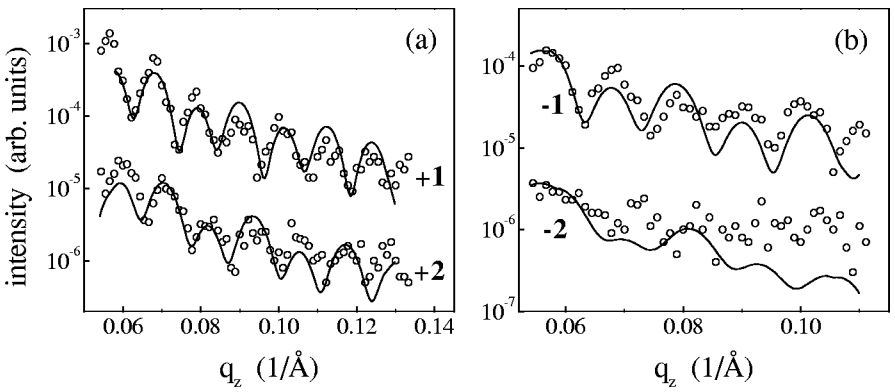

FIG. 11. Rods scans accross the first two positive GTR's (a) and first two negative GTR's (b) recorded with GID at the weak (200) RLP of sample 1.

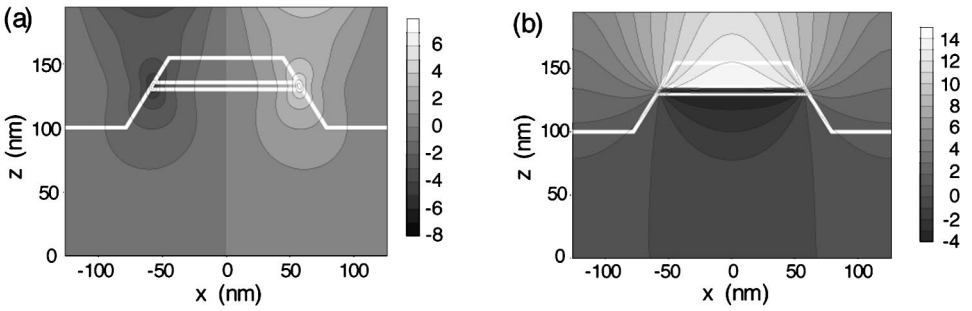

FIG. 12. FEM calculation of the displacements δx (a) and δz (b) of the grating overgrown with GaAs (sample 2). The limits of the contour bands are given in units of 10^{-3} nm. The thin white line depict the shape of the buried wire and the position of the $In_{0.03}Ga_{0.97}As$ quantum well.

metrical parameters following from the nominals. Then the theoretical diffraction intensities were fitted to the experimental data on the basis of the theory presented in Sec. III and using the simulated strain profile. Next, the strain distribution has been recalculated in accordance with the best fit of the previous iteration and the dimension parameters have been refined again. Preliminary investigations have shown the convergence of such a scheme and a sufficiency of two iterations to reach the acceptable accuracy in the framework of the approximations used in Sec. III.

The angular distance between equally spaced GTR's on the HRXRD $(q_\perp, q_z)$ map (not shown here) directly gives rough value of the lateral period of the investigated wires, and from the precise simultaneous fits of all GTR's we have found the first estimations on the vertical structure of the surface gratings, the etching depth, and the position of SQW. However, the HRXRD experiments are only weakly sensitive to the shape of the gratings because of the large penetration depth of x-rays and consequent averaging of the information from the large scale volume. To improve the estimated values and to investigate the shape of quantum wires, the GID experiments were carried out. We recorded the diffracted intensities from (220), $(\bar{2}\bar{2}0)$, and (200) Bragg reflections, performing both $q_\perp$ and q_z scans. Figures 8(a), 8(b), and 8(c) show the longitudinal (220), transverse $(\bar{2}\bar{2}0)$ and (200) $q_\perp$ scans, the experimental (dots) and theoretical (lines) curves. Due to limitations, we show the diffracted intensities recorded for only one exit angle α_f corresponding to the value $q_z = 0.044$ Å^{-1}. The (220) diffraction curves at different incidence angles α_i [Fig. 8(a)] show a visible contribution of diffusely scattered intensity appearing as wide wings at both sides of the crystal truncation rod. Their appearance is a consequence of the trapezoedric shape of the wires[25] but their intensity is caused mainly by the defects located at the wire-side walls. However, the detailed analysis of the diffuse component is out of scope of this work. Some probable reasons causing strong incoherent scattering are briefly discussed in the next section. Here, we should note that the experimental curves with evidently high contribution of diffuse scattering were excluded from the fitting procedure. By using other recorded intensities, we refined the period of the wires with high accuracy to be $D = 2550 \pm 49$ Å (see Table I).

The scans along the q_z direction were carried out at the positions of $\pm n$-order satellites to record the modulation of the separate GTRs. They are shown in Figs. 9, 10, and 11, where the panels (a) and (b) correspond to the negative and positive order GTR's, respectively. According to recent studies,[14] the GTR fringe structure contains detailed information on the shape and symmetry of the wires as well as on the depth composition of the sample. The mismatch of the maxima positions in different GTR's occurs when the wires have a trapezoidal or triangular shape, whereas the mismatching of the $+n$ and $-n$ GTR's points out the asymmetry of the wire cross-section. The absolute amplitude of GTR modulations is related to the total etching depth of the wires, and the q_z position of the maxima depend on the vertical variation of the refractive index within wires, i.e., the ordering of the layers in the multilayered stack. The transverse scan across the $\bar{2}\bar{2}0$ RLP shown in Fig. 8(b) provides a unique possibility[5,14] to investigate the geometrical parameters of the quantum wires because of the insensitivity to the strain profile of the sample. The statistically averaged values for the dimensions of the wire segments were extracted from

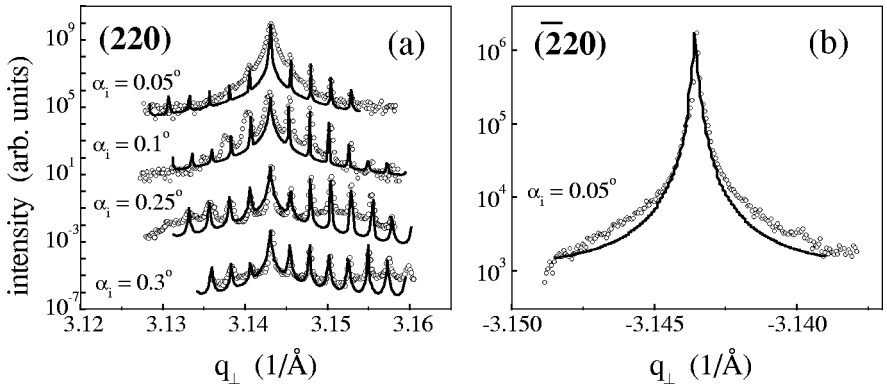

FIG. 13. Strain insensitve transverse (b) and strain sensitive longitudinal (a) in-plane scans for sample 2 recorded for different infomation depthes Λ with GID.

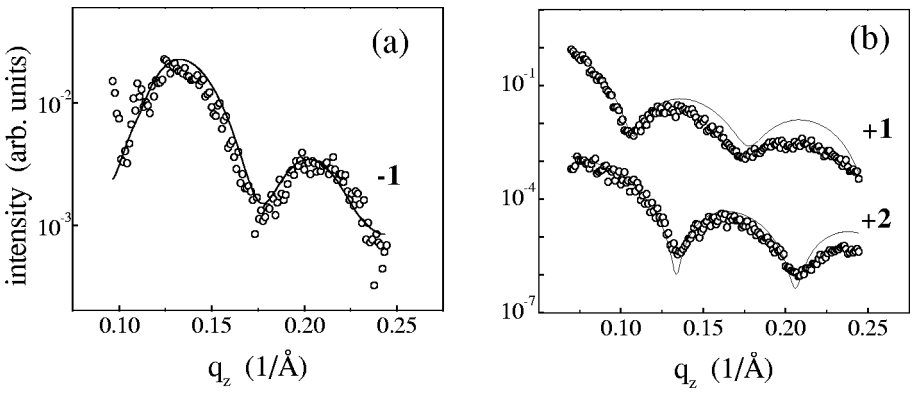

FIG. 14. Rod scans for sample 2 recorded with GID at the longitudinal (220) RLP.

the fits of experimental data. They are the lengths of the top and groove parts of wire l_{top} and l_{groove}, the thicknesses of the top, bottom and SQW layers in vertical stacking t_{top}, t_{bot}, and t_{SQW} (see Table I). All the values are found to be close to the nominals expected from the sample preparation process.

Whereas the transverse scans make it possible to study separately the shape of the QW, the longitudinal scans across the (220) Bragg reflection [Fig. 8(a), dots], being sensitive to the strains, allows a check of the validity of the FEM simulated displacement profile. The theoretical curves for the $\pm(1\div3)$ GTR's calculated with parameters from Table I and using the displacement model of FEM are plotted with solid lines in Fig. 9. The correspondence of theory and experiment appears to be satisfactory.

Finally, the GTR's of the weak (200) Bragg reflection (Fig. 11) give a measure of the scattering contrast[13] between the base compound of the wire (GaAs) and the single-quantum well ($Ga_{0.97}In_{0.03}As$) embedded into the wire. The diffraction pattern from this reflection is also sensitive to the strain profile. The phase shift induced by the SQW and the interference between surface scattered and SQW waves produce an anharmonic modulation of GTR's, typical for (200) reflection.[13,14] The oscillations of truncation rods dampen rapidly with increasing GTR order. The behavior of diffraction curves from this reflection is very sensitive to the vertical strain gradient within the undersurface region of the wires. Unfortunately the intensities of high order GTR's are too low to get satisfactory information.

B. Wires overgrown with GaAs

By the preliminary analysis of the diffraction curves recorded for Sample 2, the value of the thickness for the overgrown layer t_{over} is estimated to be approximately 400 Å. The displacement profiles $\delta z(x,z)$ and $\delta x(x,z)$ simulated by FEM are presented in Fig. 12. The edges of the quantum well of a single wire segment again play the perturbative role in the final strain distribution. A strong strain attractor at the edges of SQW induce the broad strain centers on the top of the sample surface that are clearly visible for the δx component of the atom displacements. The δz component is qualitatively similar to the displacements within Sample 1.

In Fig. 13, the recorded longitudinal (a) and transverse (b) $q_\perp$ scans are presented by open dots. For the (220) reflection we have plotted the set of diffraction curves corresponding to different incident angles $\alpha_i = 0.05°$, $0.1°$, $0.25°$, and $0.3°$. Whereas the longitudinal scans have sharp satellite peaks around the crystal truncation rod (CTR), the transverse scans across the $(\bar{2}20)$ reflection do not indicate any fine structure displaying the essential absence of any internal lateral patterning of Sample 2. Thus, the satellites of the longitudinal scans are mainly conditioned by the periodic strain distribution. The variation of the envelop function of the $q_\perp$ scans with the angle of x-ray incidence α_i directly points out the vertical gradient of the atom displacements since the angle α_i determines the penetration depth of x-rays inside the sample.[26]

The contribution of the diffusely scattered intensity causes some discrepancy between the theory based on the coherent approach and the experiment, both for transverse and longitudinal scans (Fig. 13). The variation of the incoherent component with the x-ray penetration depth seems to be connected to the inner inhomogeneity of the lattice structure. The latter may be represented by the defects network originated during the overgrowing process at the border of the wire shape, for example. Stepanov *et al.*[19] have shown that the roughness of the interfaces results in a considerable output of diffuse intensity in grazing incidence diffraction

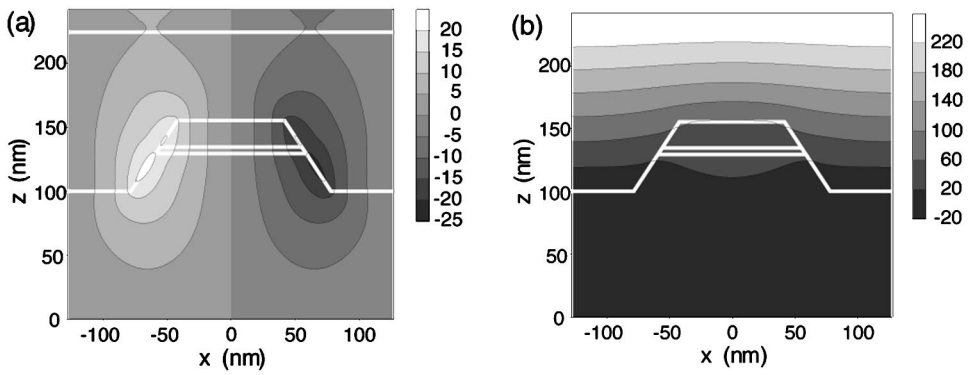

FIG. 15. FEM calculation of the displacements δx (a) and δz (b) of the grating overgrown with AlAs (sample 3). The limits of the contour bands are given in units of 10^{-3} nm. The thin white line depicts the shape of the buries wire and the position of the $In_{0.03}Ga_{0.97}As$ quantum well and the GaAs protection layer.

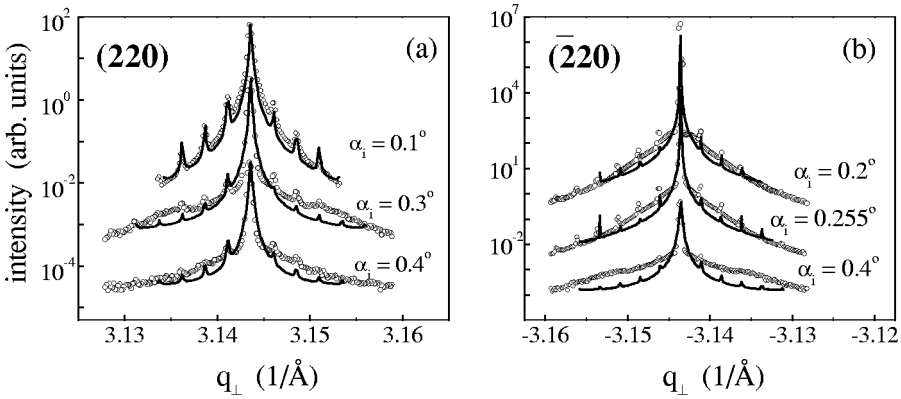

FIG. 16. Strain sensitive longitudinal (a) and strain insensitve transverse (b) in-plane scans for sample 3 recorded for different information depthes Λ with GID.

experiments. The residual roughness of the $Ga_{0.97}In_{0.03}As$ plates buried in Sample 2 also gives rise to diffuse component. In general, the spatial distribution of diffusely scattered intensity contains important information about the ordering and character of lateral imperfections.[5,19–21,27] The variation of the wing shape in Fig. 8(a) points out the vertical correlation of sample imperfections. In the case of freestanding wires, the fluctuation of the wire height can play[17] a role in the perturbation causing the incoherent scattering. Another reason for loss of coherency of x-rays is the surface roughness, in both the top and the side wall.

The grating truncation rods across the position next to the CTR satellites of the longitudinal scan are plotted in Fig. 14. The fringes of GTR's reflect the lateral periodicity of the strain centers (Fig. 12) formed by the SQW edges and spreading toward a free surface. The theory describes the data quite well with the exception of the $+1$ GTR, probably caused by inappropriate choice of $q_\perp$ for the scanning direction during the experiment.

Further iterations for sample parameters and displacement profiles refined the fitted values to ones enumerated in Table I. Theoretical simulations of the diffraction from Sample 2 show the importance of using precise atom displacement functions $\delta x(x,z)$ and $\delta z(x,z)$ for calculation of the diffraction profiles. As was found to be the case for Sample 2, the real spatial distribution of strains dominates in the formation of the diffraction pattern. Our previous attempts at modeling the displacement functions by polynomials[14] resulted in some discrepancies between theory and experiment.

C. Wires overgrown with AlAs

Sample 3 was prepared by using AlAs as overgrowth material to emphasize the scattering contrast between the original wire structure and the interwire filling. A thin GaAs cap layer (Fig. 2) was deposited to prevent the oxidation of Al on the top of the sample. The thickness of the overgrown layer was enlarged in compared with Sample 2 to suppress the induction of strain attractors on the free surface. The displacement model used to simulate x-ray diffraction is plotted in Fig. 15. Similar to Samples 1 and 2, the quantum well initiates the highly strained points where the function $\delta x(x,z)$ reaches the maximum absolute values, 0.25 Å at the left edge of the QW and -0.25 Å at the right edge. The function $\delta z(x,z)$ has no singularities and is changing gradually from the bottom to the free surface. Contrary to Sample 2, the transverse scans represented in Fig. 16(b) detect an inner lateral structure of the sample which is visible for x-rays due to the different refractive properties of GaAs and AlAs. Both in longitudinal (220) and transverse $(\bar{2}20)$ scans, the clearly visible wings to the left and right of the fundamental Bragg peak indicate a diffuse component of x-ray scattering. The satellite peaks are not so pronounced as for previous samples because of the thick AlAs overlayer covering the wires, and GTR satellites in longitudinal scans are sharper than in transverse ones. This fact can be explained by the additional sensitivity of longitudinal scans to the strains, as noted above. The periodic strains inside the sample are distributed along the entire depth of the grating segment, whereas the shape contrast region influencing the transverse curves is located at the bottom part of the sample cross section.

Figure 17 shows the GTR's of the positive (a) and negative (b) orders from (220) reflection, experimental (open dots) and theoretical (solid lines) curves. The fringes of the truncation rods are observed to be damped considerably due to heavy overgrowth of wires. The slow oscillation of CTR is

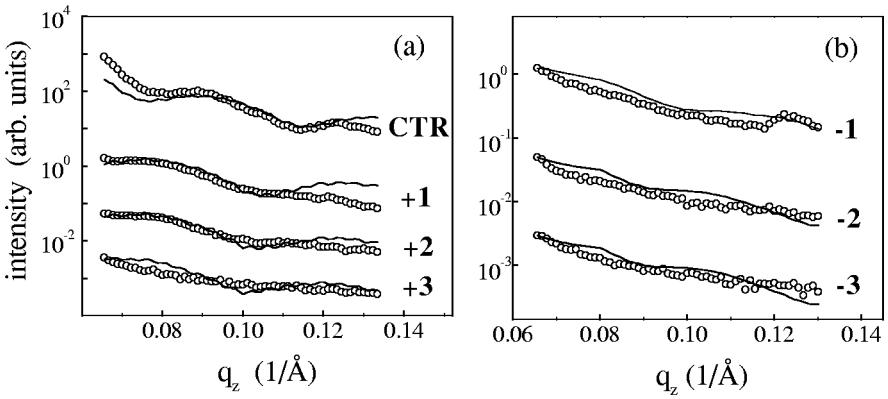

FIG. 17. Rod scans accross the $+1$st to $+3$rd GTR (a) and -1st to -3rd GTR (b) recorded with GID at the longitudinal (220) RLP of sample 3.

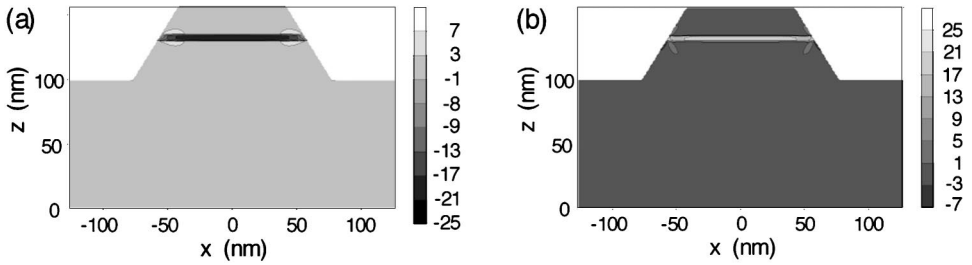

FIG. 18. Strain distribution $\epsilon_{xx}(x,z)$ and $\epsilon_{zz}(x,z)$ of sample 1 calculated by FEM by refinement of a model structure shown in Fig. 2(a). The distances between the contour lines are given in units of 10^{-4}.

determined mainly by the cap thickness of GaAs layer ($t_{\mathrm{cap}} = 165$ Å). The weak sensitivity of the simulated GTRs to the thickness of AlAs allowed us to estimate the approximate value for this parameter, $t_{\mathrm{over}} \sim 700$ Å. The fitted parameters of the wire's shape are presented in Table I.

V. DISCUSSION

Based on the displacement fields of the refined model structures shown in Fig. 2, the rocking curve simulations show sufficient agreement with experiment. Consequencies for electronic properties should be discussed in terms of the spatial strain distribution being available via FEM output as the displacement fields. The strain distribution of a freestanding wire structure has been already studied by DeCaro *et al.*[28] We focus our attention on the variation of strain induced by the overgrowth process. Unfortunately, the overgrown samples investigated here did not show sufficient PL intensity emitted from the $In_{0.03}Ga_{0.97}As$ SQW. This may be caused by the defects incorporated during the cleaning process before, or the defect migration during, the overgrowth process. Thus we will discuss the consequences of strain relaxation qualitatively. As shown in Fig. 1 the redshift found at freestanding wire structures becomes overcompensated after the overgrowth.

The energy shift of the SQW within a quantum wire consists mainly of two contributions

$$\Delta E = \Delta E(L_{\mathrm{x}}, L_{\mathrm{z}}) + \Delta E(\epsilon_{nm}), \tag{24}$$

the energy shift caused by quantization (the first term) and the strain-induced shift (the second term). Both contributions show contradictory behavior. For the investigated structures the first one causes a blueshift, whereas the second term causes a redshift.

The quantization energy of the levels are described by the formula

$$\Delta E_{l,n}(\mathbf{k}) = \frac{\hbar^2 \pi^2}{2}\left(\frac{l^2}{m_{\mathrm{x}}^* L_{\mathrm{x}}^2} + \frac{n^2}{m_{\mathrm{z}}^* L_{\mathrm{z}}^2}\right) + \frac{\hbar^2 k_{\mathrm{y}}^2}{2 m_{\mathrm{y}}^*}, \tag{25}$$

where m_{i}^* denote the directionally dependent effective masses. For the lowest energy levels ($n=1,\ l=1$) and fixed vertical thickness of the SQW L_{z}, the quantization energy and consequently the energy gap between electron and (heavy) hole level varies as $\sim 1/L_{\mathrm{x}}^2$ with the wire width L_{x}. This behavior was already verified.[29]

The change of the electronic band gap of SQW material by strain is described by the defomation potential approach introduced by Kane, [30] van der Walle,[31] and others. Following Kash *et al.*[32] the strain-induced shift of the band edges of the conduction and valence bands along [001] at the Γ point are given by

$$\Delta E_{c,v} = a(\epsilon_{xx} + \epsilon_{zz}) \pm (\alpha^2 + \beta^2 + \gamma^2)^{1/2} \tag{26}$$

using

$$\alpha = \frac{1}{2}A + b\left(\frac{1}{2}\epsilon_{xx} - \epsilon_{zz}\right),\quad \beta = \frac{1}{2}\sqrt{3}\, b\, \epsilon_{xx},\quad \gamma = d\,\epsilon_{xz},$$

where a denotes the hydrostatic and b, d the shear deformation potentials, respectively, following the notation of Bir and Pikus, [2] ϵ_{nm} are the diagonal and shear elements of the strain tensor, respectively. The parameter A describes the effect of splitting the twofold degeneracy of heavy- and light-hole bands.[2] Because the absolute strains are small and data of deformation potential constants published in the literature differ (see references in Köpf *et al.*[33]), we neglect the shear components of the deformation potentials in Eq. (26) for a very rough estimation of the upper level of the expected electronic effect.

Due to the given wire geometry, the component ϵ_{yy} is a constant independent of the vertical structure of the sample (not shown here). Within the SQW the strain values $\epsilon_{yy} = \epsilon_{xx} = -2.1\times 10^{-3}$ and $\epsilon_{zz} = +1.9\times 10^{-3}$ coincide with expected values for pseudomorphic strain.

The $\epsilon_{xx}(x,z)$ and $\epsilon_{zz}(x,z)$ strain distributions of the freestanding wire structure are shown in Fig. 18. Both ϵ_{xx} and ϵ_{zz} reach a maximum within the SQW and amount to -1.99×10^{-3} and $+1.6\times 10^{-3}$, respectively. These values indicate only small relaxation and both strains show a steep strain gradient towards the wire-side planes. About 80% of the SQW exhibits nearly uniform strain and should initiate an uniform shift of the band-gap energy. The appearance of a small surface region with strongly varying strain was already found by DeCaro *et al.*[28] It is mainly caused by the influence of shear components and the influence of the piezoelectric effect. This finding was verified experimentally by Shen *et al.*[34] measuring the **q** dependence of the lattice strain at various in-plane x-ray Bragg reflections. Under the restrictions mentioned above we expect a strain-induced shift of about $\Delta E \approx 1.5$ meV with respect to the pseudomorphically strained mesa using $a \approx -6$ eV. This corresponds qualitatively to the measured redshift shown in Fig. 1. For etched dots containing 3% indium we found a line shift in similar order of magnitude.[4]

As shown in Fig. 18 strain interaction between SQW and the cladding layers appears mainly at the side planes close to the interfaces between the SQW and the GaAs cladding layers. The average values of in-plane and out-of plane strain are available from the shift of the envelope function of scat-

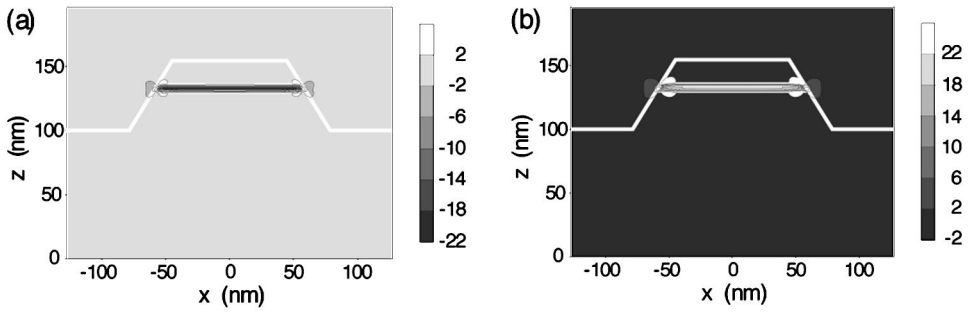

FIG. 19. Strain distribution $\epsilon_{xx}(x,z)$ and $\epsilon_{zz}(x,z)$ of sample 2 calculated by FEM by refinement of a model structure shown in Fig. 2(b).The distances between the contour lines are given in units of 10^{-4}.

tering intensity [see Figs. 7, 8(a), and 8(b)]. The strain distribution becomes available only via accompanied FEM assisted rocking curve simulations.

Figure 19 shows the strain distribution of Sample 2. In the same way as for Sample 1, the strain is maximum within the SQW even after GaAs overgrowth. Both numbers ϵ_{xx} and ϵ_{zz} equal approximately to the respective values for the free-standing wire sample.

Compared with Sample 1 the overgrown sample shows a reduced width of strong strain variation and a smaller amount of the strain gradient close to the former wire-side planes. Accompanied with the passivation of nonradiative defects the overgrown sample should show a much enhanced PL intensity. This was found for various other samples of similar composition[4] but not at the presently investigated ones. Also, our findings do not verify the nearly complete compensation of the redshift shown in Fig. 1.

Nevertheless, as recently found,[15] the strain modulation within the overlayer induced by growth onto a laterally patterned substrate appears at the sample surface. Within the GaAs, the strain is tensile above the former wires but compressive in between. Due to the low indium content within the SQW, the induced strain modulation is not larger than $\Delta\epsilon_{xx}\approx 3\times 10^{-4}$, corresponding to a gap variation smaller than 2 meV. The strongest strain fluctuations of GaAs appear at the in-plane interfaces close to the SQW. They may act as centers for defect migration and for nonradiative recombination of charge carriers. The variation of the average in-plane strain with depth is displayed in Fig. 13(b). For very small α_i the rocking curve appears rather symmetrical because the residual strain is nearly canceled below the surface. For larger α_i the envelope of the intensity distribution shifts to larger $q_\perp$ due to the compressive strain of the SQW.

Figure 20 shows the strain distribution of the sample overgrown with AlAs. Here, the strain discussion is more complicated due to the termination of strain by the GaAs cap layer. Due to the larger lattice parameter of AlAs compared with GaAs, the induced strains become larger within the SQW. The values are $\epsilon_{xx}=-2.5\times 10^{-3}$ and $\epsilon_{zz}=+2.5\times 10^{-3}$ and are rather uniformly distributed over the entire volume of the SQW. The region of high strain gradient in the vicinity of the SQW side planes is small. The expected change in the gap energy is $\Delta E\approx 2.5$ meV with respect to the mesa. Unfortunately, this sample also did not show radiative recombination, which could verify our assumptions. However, strong strain variations appear close to the GaAs layers embedding the SQW. Within the AlAs overlayer, the lateral strain modulation is about 50% and remains nearly uniform with depth. This behavior is terminated by the GaAs top layer. Here, lateral strain modulation still appears but it is much smaller then in AlAs (see Fig. 20).

This rather complicated strain distribution is difficult to resolve from visual inspection of longitudinal-scan rocking curves. For $\alpha_i<\alpha_c$ only the GaAs top layer is inspected. Due to the nearly vanishing absolute strain of the cap layer, the scattered intensity appears rather symmetric. With increasing information depth Λ the rocking curve becomes slightly asymmetric. The GTR intensity at larger $q_\perp$ is slightly higher compared with the low $q_\perp$ side. This fact reflects the compressive in-plane strain of the AlAs region and the SQW at larger Λ. It should be noted that the appearance of GTR satellites in the longitudinal scans of Samples 2 and 3 are mainly caused by the lateral strain modulation within the respective overlayers. The GTR's disappear completely in the transverse scans of Sample 2. That is caused by the vanishing lateral density modulation of this sample (GaAs on GaAs; the thin SQW may be neglected in this case). The visible GTR's in the transverse scan of Sample 3 may be explained by a strain-induced Ga segregation during the AlAs overgrowth, or by the remaining density difference between GaAs and AlAs in deeper regions of the sample.

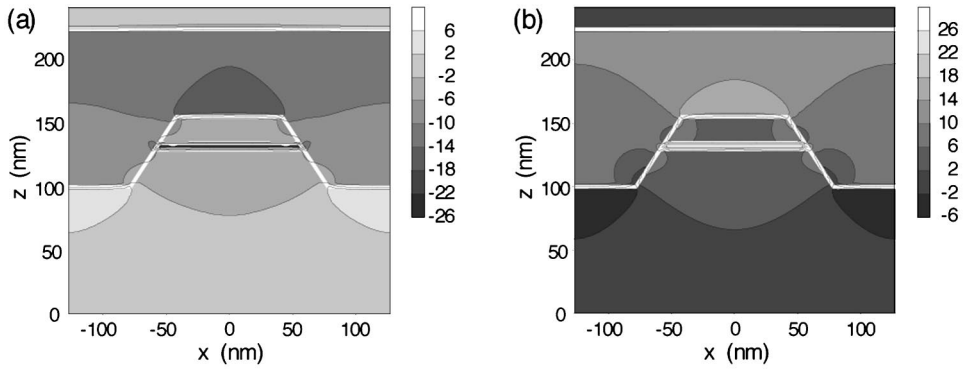

FIG. 20. Strain distribution $\epsilon_{xx}(x,z)$ and $\epsilon_{zz}(x,z)$ of sample 3 calculated by FEM by refinement of a model structure shown in Fig. 2(c).The distances between the contour lines are given in units of 10^{-4}.

VI. CONCLUSION

In the present paper, we performed a detailed strain anlysis of freestanding and overgrown lateral nanostructures containing a low strained $In_xGa_{1-x}As$ SQW. Our findings verify the results of respective PL experiments that show a much higher PL intensity for overgrown samples compared with freestanding ones. This is caused by the small strain interaction between SQW and the cladding layers and the repulsion of the strain gradient close to the the wire side walls. The extension of the uniform strain volume and the passiviation of centers for nonradiative recombination justify the attempt of an additional growth step in the device technology.

ACKNOWLEDGMENTS

The authors thank the VW Foundation (Grant No. I 70/588) and the ESRF for financial support.

*Present address: Rigaku Corp., 3-9-12 Matsubara, Akishima, Tokyo 196, Japan

†Author to whom correspondence should be addressed. FAX: +49 0331 1133. Electronic address: upietsch@rz. uni-potsdam.de

[1] D. Bimberg, M. Grundmann, and N. N. Ledentsov, *Quantum Dot Heterostructures* (Wiley, Chichester, 1999).

[2] G. Bir and G. Pikus, *Symmetry and Strain-induced Effects in Semiconductors* (Wiley, Chichester, 1974).

[3] R. Steffen, Ph.D. thesis, University of Würzburg, Würzburg, 1996.

[4] K. H. Wang, Ph.D. thesis, University of Würzburg, Würzburg, 1998.

[5] V. Holý, U. Pietsch, and T. Baumbach, *X-ray Scattering by Thin Films and Multilayers* (Springer-Verlag, Berlin, 1998).

[6] L. Tapfer and P. Grambow, Appl. Phys. A: Solids Surf. **50**, 3 (1990).

[7] V. Holý, A. A. Darhuber, G. Bauer, P. D. Wang, Y. P. Song, C. M. Sotomayor Torres, and M. C. Holland, Phys. Rev. B **52**, 8384 (1995).

[8] G. T. Baumbach and M. Gailhanou, J. Phys. D **28**, 2321 (1995).

[9] Q. Shen, S. W. Kycia, E. S. Tentarelli, W. J. Schaff, and L. F. Eastman, Phys. Rev. B **54**, 16 381 (1996).

[10] D. Lübbert, T. Baumbach, S. Ponti, U. Pietsch, L. Leprince, J. Schneck, and A. Talneau, Europhys. Lett. **46**, 479 (1999).

[11] D. Lübbert, B. Jenichen, T. Baumbach, H. T. Grahn, G. Paris, A. Mazuelas, T. Kojima, and S. Arai, J. Phys. D: Appl. Phys. **32**, A21 (1999).

[12] N. Darowski, U. Pietsch, Y. Zhuang, S. Zerlauth, G. Bauer, D. Lübbert, and T. Baumbach, Appl. Phys. Lett. **73**, 806 (1998).

[13] N. Darowski, K. Paschke, U. Pietsch, K. H. Wang, A. Forchel, D. Lübbert, and T. Baumbach, Physica B **248**, 104 (1998).

[14] A. Ulyanenkov, T. Baumbach, N. Darowski, U. Pietsch, K. H. Wang, A. Forchel, and T. Wiebach, J. Appl. Phys. **85**, 1524 (1999).

[15] N. Darowski, U. Pietsch, U. Zeimer, V. Smirnitzki, and F. Bugge, J. Appl. Phys. **84**, 1366 (1998).

[16] D. K. G. de Boer, Phys. Rev. B **53**, 6048 (1996).

[17] Q. Shen, C. C. Umbach, B. Weselak, and J. M. Blakely, Phys. Rev. B **53**, R4237 (1996).

[18] Q. Shen, Acta Crystallogr., Sect. A: Found. Crystallogr. **42**, 525 (1986).

[19] S. A. Stepanov, E. A. Kondrashkina, M. Schmidbauer, R. Köhler, J. U. Pfeiffer, T. Jach, and A. Yu. Souvorov, Phys. Rev. B **54**, 8150 (1996).

[20] V. Holý and T. Baumbach, Phys. Rev. B **49**, 10 668 (1994).

[21] V. M. Kaganer, R. Köhler, M. Schmidbauer, R. Opitz, and B. Jenichen, Phys. Rev. B **55**, 1793 (1997).

[22] A. Gonis, *Green Functions for Ordered and Disordered Systems* (North-Holland, Amsterdam, 1992).

[23] G. T. Baumbach, D. Lübbert, U. Pietsch, N. Darowski, L. Leprince, A. Talneau, and J. Schneck, Physica B **248**, 343 (1998).

[24] M. Born and E. Wolf, *Principles of Optics* (Pergamon, London, 1959).

[25] T. Baumbach and D. Lübbert, J. Phys. D **32**, 726 (1999).

[26] H. Dosch, B. W. Batterman, and D. C. Wack, Phys. Rev. Lett. **56**, 1144 (1986).

[27] A. Ulyanenkov, Appl. Phys. A: Mater. Sci. Process. **66**, 193 (1998).

[28] L. DeCaro, L. Tapfer, and A. Giuffrida, Phys. Rev. B **54**, 10 575 (1996).

[29] A. Forchel, R. Steffen, T. Koch, M. Michel, M. Albrecht, and T. L. Reinecke, Semicond. Sci. Technol. **11**, 1529 (1996).

[30] E. Kane, Phys. Rev. **178**, 1368 (1970).

[31] C. Van der Walle, Phys. Rev. B **39**, 1871 (1989).

[32] K. Kash, B. P. Van der Gaag, D. D. Mahoney, A. S. Gozdz, L. T. Florez, J. P. Harbison, and M. D. Struge, Phys. Rev. Lett. **67**, 1326 (1991).

[33] Ch. Köpf, H. Kosina, and S. Selberherr, Solid-State Electron. **41**, 1139 (1997).

[34] Q. Shen and S. Kycia, Phys. Rev. B **55**, 15 791 (1997).